INTERNATIONAL JOURNAL FOR NUMERICAL METHODS IN FLUIDS
Int. J. Numer. Meth. Fluids 2007; **54**:517–541
Published online 12 December 2006 in Wiley InterScience (www.interscience.wiley.com). DOI: 10.1002/fld.1408

Large eddy simulation of turbulent flow in a true 3D Francis hydro turbine passage with dynamical fluid–structure interaction

Lixiang Zhang[1,*,†,‡], Yakun Guo[2,§] and Wenquan Wang[1]

[1]*Department of Engineering Mechanics, Kunming University of Science and Technology, Kunming 650051, Yunnan, China*
[2]*Department of Engineering, University of Aberdeen, Aberdeen AB24 3UE, U.K.*

SUMMARY

Results are described from a combined numerical and laboratory model study of the turbulent flow in a true 3D blade passage of a Francis hydro-turbine. The large eddy simulation (LES) is applied to investigate the intrinsic features and the spatial and temporal variations of the flow structures in the blade passage with strong wakes in inflow sweeping and the turbulence-induced blade vibration. The flow passes through the vibrating boundaries. Therefore, the system under consideration is in a dynamic fluid–structure interaction (FSI). In the simulation, one-coefficient dynamic sub-grid scale (SGS) model is incorporated in LES with Reynolds number 148 400 to better describe the energy exchange mechanism between large and small scales under the influences of strong geometrical curvature and vibrating boundaries. The governing equation of the blade vibration with FSI has been established by generalized variational principle combining the fluid and the structure. The vibration analysis is carried out by using Wilson-θ method. Separate iteration schemes are applied to solve the flow and the vibration in turn. The pressures on the wall sides of the blade and its vibrating accelerations are simultaneously measured. The numerical results show that the temporal and spatial distributions of turbulence in the 3D blade passage are significantly influenced by the curvature of blade configuration, the blade vibration, and the distorted wakes generated by flow passing through guide vanes. The influences of the vibration on the near-wall flow structures are quite remarkable. The simulated results are favourably compared with the measurements. Copyright © 2006 John Wiley & Sons, Ltd.

Received 13 April 2006; Revised 2 October 2006; Accepted 15 October 2006

KEY WORDS: turbulent flow; large eddy simulation; fluid–structure interaction; hydro turbine; flow measurement

*Correspondence to: Lixiang Zhang, Department of Engineering Mechanics, Kunming University of Science and Technology, 50 East Ring Road Kunming 650051, Yunnan, China.
†E-mail: zlxzcc@126.com
‡Professor.
§Lecturer.

Contract/grant sponsor: National Natural Science Foundation of China (NSFC); contract/grant numbers: 90210005, 50579025

1. INTRODUCTION

A blade passage of a Francis hydro turbine is highly spatially skewing consisting of blades, the top-crown, and the bottom-ring. The high-speed flow entering into the blade passage at the entrance with an angle of attack rotates the runner of a machine unit by strong interaction, which transfers the water energy to the blades for electricity generation. In this energy exchange process, rapid variation of the flow pattern in the blade passage results in a complicated, non-uniform and unsteady turbulent flow. So far, most 3D numerical simulations of the turbulent flows in the 3D blade passage have been performed based on RANS incorporated the k–ε family models for engineering purpose [1, 2]. These studies have not investigated the turbulent mechanisms and the spatial and temporal distributions of turbulent flow in a strong 3D blade passage. Though a few direct numerical simulation (DNS) studies based on the linear blade cascade simplifications [3–6] have been recently conducted to investigate the turbulent flows in the blade passage for a low-pressure turbine (LPT), knowledge on flows in a true Francis turbine is still lacking and substantial research is required. In principle, DNS is the most powerful tool to study the turbulent flows [7], however, the huge requirement for computing resources for simulating a strong 3D flow with a high Reynolds number limits its application in many engineering and industrial flows. Recent study of Rodi [6] shows that LES incorporated with a dynamical sub-grid scale (SGS) model, whose computing cost is much lower than DNS, can obtain comparably good results as DNS for many engineering and industrial problems. Therefore, LES is adopted in this study to fulfil the simulation of the complex turbulent flow in Francis blade passage.

In the past decade, LES has been widely used and well developed into a good tool for simulating turbulent flow in complex geometrical passage. Incorporating some computing techniques, such as body-fitted curvilinear, unstructured grid and low-order dissipation as well as non-energy conserving discretization, LES has been successfully used to solve problems [8–10] and to simulate many turbulent flows with some complex geometry [11–15]. However, the successful application of LES to the very complex practical turbulent flows is still lacking and remains as a challenging task to researchers. For example, to our knowledge, there have not been any reports of numerical simulations using LES in a true 3D Francis hydro-turbine passage with FSI. On one hand, the generation of high-quality body-fitted curvilinear meshes even in simple geometries may require proper grid embedding/multi-domain techniques, thus significantly increasing the cost of the computations [16]. On the other hand, the use of unstructured grids for simplifying grid generation has a negative impact on the stability and convergence of the algorithms for a complex geometry, consequently largely increasing the numbers of operations per node. Furthermore, the application of moving and/or deforming boundaries that are usually encountered in engineering problems and solved by using ALE [17–19] to treat the change of meshes, results in additional computational effort. The flow-induced vibration [20, 21], treated as vibrating boundaries in this study, is very difficult to deal with in FSI system while computational fluid dynamics (CFD) plays an important role in the progress. This study, therefore, is motivated by exploring a more practical methodology that can better perform CFD task for a complex geometry (e.g. 3D blade passage of Francis turbine) with FSI.

The focus of this paper is on simulating the turbulent flow in a strong 3D blade passage of Francis turbine. Strongly distorted wakes caused by guide vanes and flow-induced vibrations of the blade are taken into account under dynamical FSI by combining LES and Wilson-θ method [22] based on the finite element method (FEM). In LES, a dynamic SGS model is applied to better simulate energy exchange mechanisms between the large and small scales due to strong 3D geometrical curvature when the blades are vibrating. To validate the model developed here

DOI: 10.1002/fld

a laboratory experiment is conducted. The pressures on both sides of the vibrating blade and its vibrating accelerations were simultaneously measured using LL-072-25A pressure transducers manufactured by Kulite Inc. of U.S.A. and DH201 accelerators made by DonghuaTest Inc. of China, respectively. The flow simulations with FSI are favourably compared with the experiments, though there exists a difference for some details of the history.

2. NUMERICAL MODEL

2.1. Problem descriptions

The object under consideration is a true model Francis turbine of type A55x having a runner of 450 mm diameter with 10 blades. To identify the intrinsic turbulence due to the geometrical shape of the strong 3D blade passage and to focus the study on the influences of the vibration on the flow the rotation of the unit is not considered at this stage. Upstream wakes that traverse the inlet of the passage are produced by the moving guide vanes, by which the direction of the coming flow is adjusted. The incident angle of the main flow and the velocity at the inlet of the passage are controlled with the opening of the guide vanes. For the present study, the opening of the guide vanes is 22 mm, the incident angle of the main flow is 38.7° and the mean velocity of coming flow based on the inlet surface of the passage is $U_{\text{ref}} = 1$ m/s (referred to as reference velocity). The Cartesian system x_1-, x_2- and x_3-axis refer to the axial, tangential and span-wise directions, respectively (see Figure 1). The short and long edges of the blade along the span-wise direction, referred as leading and trailing edges, are $L_1 = 166$ mm and $L_2 = 281$ mm. The crossing lines with the top-crown and the bottom-ring are $L_3 = 130$ mm and $L_4 = 197$ mm, and the chord length $L = 157.3$ mm. The pitches of the blades are $S_1 = 69$ mm (at the top) and $S_2 = 102$ mm (at the bottom) at the location of the inlet. The relative height of the blade passage is $x_3/L = 2.85$, and the mean blade pitch at the inlet $x_2/L = 0.543$. The Reynolds number is $Re = U_{\text{ref}}L/\nu = 148\,400$ (ν is kinetic viscosity of water at temperature of 18°C). Due to the periodical symmetry and for the consideration of computational cost, only one blade passage is considered in this paper. The computational domain with inflow and outflow regions is shown in Figure 1.

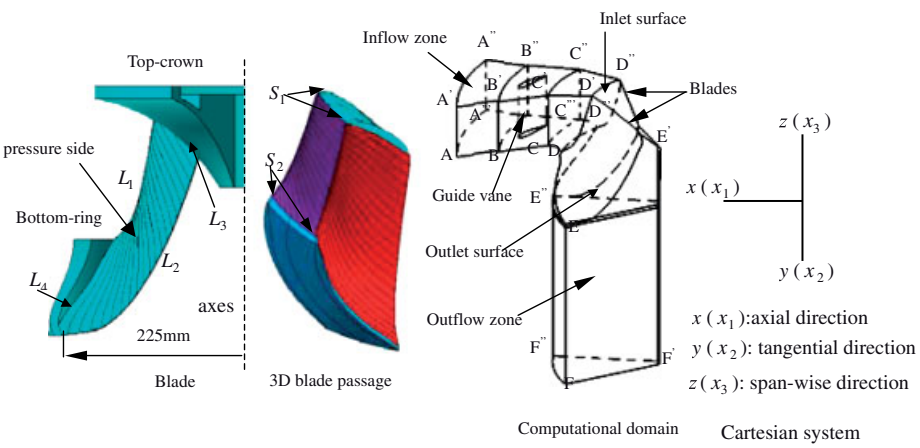

Figure 1. Blade passage configuration and computational domain.

DOI: 10.1002/fld

2.2. Grid generation

The objective of this paper is to examine the build-up turbulence features in a strong 3D blade passage and to investigate the spatial and temporal natures of the vortex structures due to the guide vanes induced wakes and the vibrating blades. For such complicated configuration of the computational domain, non-uniform and non-structured meshes of both H- and T-type cells are used with refinement in near wall regions for accurately representing the small-scale structures and ensuring simulation accuracy. Based on flow the Reynolds number is investigated, the first cell size near the walls of the blade is determined on the principle [23] that it should be generally less than $c(\Delta x_1\,\Delta x_2\,\Delta x_3)^{1/3}$, where c is taken as 0.1 for the mesh under consideration. The distances (in pitch-wise direction) of the first grid points away from the walls are 0.1 mm for the suction side and 0.08mm for the pressure side, respectively. This is equivalent to that the dimensionless wall distance y^+ is less than 3 wall units in pitch-wise direction for $Re = 148\,400$. The sizes of the grid cells are from 0.7 to 1.4 mm, corresponding to the dimensionless sizes of the cells being 13–66 wall units. Consequently, the total number of the grid points within the blade passage domain is about $200 \times 140 \times 105(L_2 \times L_4 \times S_2)$, i.e. approximately 3.0 million, in which the grid along pitch-wise direction is gradually refined towards the blades. The grid points in the regions of the inflow and outflow become gradually coarser with the number of the points being about 1.2 million. The total grid points are 4.2 million in the computational domain (see Figure 1).

2.3. Governing equations

The governing equations of the incompressible viscous flow in a Francis hydro-turbine passage are operated by a Gaussian filter to separate the large scale from the small-scale eddies and can be written as

$$\frac{\partial \overline{u}_j}{\partial x_j} = 0 \tag{1}$$

$$\frac{\partial \overline{u}_i}{\partial t} + \frac{\partial}{\partial x_j}(\overline{u}_i \overline{u}_j) = -\frac{\partial \overline{P}}{\partial x_i} - \frac{\partial \tau_{ij}}{\partial x_j} + \nu \frac{\partial}{\partial x_j}\left(\frac{\partial \overline{u}_i}{\partial x_j}\right) - 2\omega \varepsilon_{i3k} \overline{u}_k \tag{2}$$

in which $\tau_{ij} = \overline{u_i u_j} - \overline{u}_i \overline{u}_j$ is the SGS stresses of the effect from the small scales, $\overline{u}_i$ the filtered velocity in i direction, $\overline{P} = \overline{p} - \omega^2 r^2/2$ and $\overline{p}$ the pressure (divided by the fluid mass density), ν the kinetic viscosity, ω the angular velocity which rotates around the x_3-axis, r the rotating radius with respect to the x_3-axis, ε_{i3k} a circular replacement tensor. Note that the presence of the curvature varying blade walls, particularly when they are vibrating, affects significantly the physics of the SGSs stresses and inhibits greatly the natural growth of the small scale structures. Therefore, the energy exchange mechanisms between the resolved and unresolved structures may be significantly altered compared to those that flow in flat and straight channels. Thus, to better simulate such energy exchange mechanisms, it is essential to update the model coefficients during the computation instead of using constants, as the classical Smagorinsky's model does. Furthermore, a one-coefficient dynamic SGS model [24] is adopted in this study to improve the energy transfer relationship between the large and small scales in the true hydro-turbine blade passage. For convenience and completeness, we give a brief and simple description to one-coefficient dynamic SGS model. We first consider an eddy-viscosity model to parameterize both subgrid

DOI: 10.1002/fld

and subtest stresses, namely

$$\tau_{ij} = -2c_d\alpha_{ij} \tag{3}$$

$$T_{ij} = -2c_d\beta_{ij} \tag{4}$$

in which $T_{ij} = \overline{\overline{u_i u_j}} - \overline{\overline{u}}_i\overline{\overline{u}}_j$ is the subtest stresses, which are obtained by applying a test filter $\overline{\overline{G}}$ with a characteristic width $\overline{\overline{\Delta}} = 2\overline{\Delta}$, to the Navier–Stokes equations. The dynamic adjustment of the model coefficients is based on the following identity:

$$L_{ij} = \overline{\overline{u_i u_j}} - \overline{\overline{u}}_i\overline{\overline{u}}_j \equiv T_{ij} - \overline{\overline{\tau}}_{ij} \tag{5}$$

in which $\overline{\overline{\tau}}_{ij}$ is SGS stresses based on the test filter $\overline{\overline{G}}$ to the Navier–Stokes equations. An error function is introduced as

$$e_{ij} = L_{ij} - T_{ij} + \overline{\overline{\tau}}_{ij} \tag{6}$$

The least-squares method is used to minimize the error and the dynamic model coefficient is obtained as

$$c_d = -\frac{1}{2}\frac{\langle(\overline{\overline{u_i u_j}} - \overline{\overline{u}}_i\overline{\overline{u}}_j)(\beta_{ij} - \overline{\overline{\alpha}}_{ij})\rangle}{\langle(\beta_{ij} - \overline{\overline{\alpha}}_{ij})(\beta_{ij} - \overline{\overline{\alpha}}_{ij})\rangle} \tag{7}$$

Thus, the dynamic model used in this study is stated as

$$\tau_{ij} - \frac{\delta_{ij}}{3}\tau_{kk} = -2\nu_T\overline{S}_{ij} = -2c_d\overline{\Delta}^2(2\overline{S}_{ij}\overline{S}_{ij})^{1/2}\overline{S}_{ij} \tag{8}$$

in which δ_{ij} is Kronecker's delta and bar(s) over the variables represent(s) filtered.

2.4. Boundary conditions

The most distinctive geometry feature of a Francis hydro-turbine is the repetitiveness of blades in pitch-wise direction. For the Francis turbine blade passage studied in this paper, 10 blades are periodically located along the pitch-wise direction with the circumference angle of a blade of 36°. The pitch-to-chord ratio is 0.544, which is significantly larger than the length scale of the turbulent eddies inside blade boundary layer, and bigger than the guide vanes induced wakes scale. The periodic boundary treatment is innocuous in the artifice periodicity when the boundary surface pairs of ABCDD′C′B′A′ at the inflow zone and of EFF′E′ at the outflow zone (see Figure 1) are treated as statistically and instantaneously periodic boundary conditions, although the turbulent flow does not satisfy periodicity. This is well suitable for an artifice using a blade passage [3–6].

No-slip conditions are imposed on the rigid boundaries, i.e. D′C′B′A′A″B″C″D″ at the inflow zone, FEE″F″, D‴E″ED, and the surrounding surface of the guide vane. The velocity on the surface of the inflow (AA′A″A‴) is specified as a steady incoming flow condition. An initial turbulent kinetic energy (TKE) is added based on the measured fluctuating velocity in the water supply pipe. On the outlet surface of the outflow region (FF′F″) Neumann condition, $\partial\phi/\partial n = 0$, is applied, where ϕ is a flow variable and n an outward normal of the surface.

One of the interests of this paper is to consider the influences of the vibrating blades on the turbulent flow in the blade passage. To this end, the blade is treated as an elastic structure, clamped

DOI: 10.1002/fld

at two ends with the top-crown and the bottom-ring. The blade vibrates under excitation of the turbulent flow. Thus, on the pressure and suction sides of the blade, the interaction conditions for the motion between the flow and the blade vibration can be written as

$$u_i^{\mathrm{fs}} - \dot{v}_i^{\mathrm{fs}} = 0 \tag{9}$$

in which $\dot{v}_i$ is the vibration velocity of the blades, the dot over the variable represents the derivative with respect to time, the superscript fs indicates the interface between the fluid and the structure (blade). After implementing a lengthy operation based on the generalized variational principle of the FSI system, the dynamic coupling conditions between the flow and the structure, as a FEM formulation, are obtained as

$$\begin{bmatrix} \mathbf{m}^{00} & \mathbf{m}^{01} & \mathbf{m}^{02} \\ \mathbf{m}^{10} & \mathbf{m}^{11} & \mathbf{m}^{12} \\ \mathbf{m}^{20} & \mathbf{m}^{21} & \mathbf{m}^{22} \end{bmatrix} \begin{pmatrix} \ddot{\mathbf{v}}^0 \\ \ddot{\mathbf{v}}^1 \\ \ddot{\mathbf{v}}^2 \end{pmatrix} + \begin{bmatrix} \mathbf{c}^{00} & \mathbf{c}^{01} & \mathbf{c}^{02} \\ \mathbf{c}^{10} & \mathbf{c}^{11} & \mathbf{c}^{12} \\ \mathbf{c}^{20} & \mathbf{c}^{21} & \mathbf{c}^{22} \end{bmatrix} \begin{pmatrix} \dot{\mathbf{v}}^0 \\ \dot{\mathbf{v}}^1 \\ \dot{\mathbf{v}}^2 \end{pmatrix} + \begin{bmatrix} \mathbf{k}^{00} & \mathbf{k}^{01} & \mathbf{k}^{02} \\ \mathbf{k}^{10} & \mathbf{k}^{11} & \mathbf{k}^{12} \\ \mathbf{k}^{20} & \mathbf{k}^{21} & \mathbf{k}^{22} \end{bmatrix} \begin{pmatrix} \mathbf{v}^0 \\ \mathbf{v}^1 \\ \mathbf{v}^2 \end{pmatrix}$$
$$= - \begin{pmatrix} 0 \\ \mathbf{q}^{11}\mathbf{u}^1 + \mathbf{g}^{11}\mathbf{p}^1 \\ \mathbf{q}^{22}\mathbf{u}^2 + \mathbf{g}^{22}\mathbf{p}^2 \end{pmatrix} \tag{10}$$

or, as a compact matrix notation

$$\mathbf{M}\ddot{\mathbf{v}} + \mathbf{C}\dot{\mathbf{v}} + \mathbf{K}\mathbf{v} = \mathbf{R} \tag{11}$$

in which the bold letters represent matrices; **m** is the mass matrix of the structure; **c** the damping matrix; **k** the stiffness matrix; **v**, $\dot{\mathbf{v}}$ and $\ddot{\mathbf{v}}$ the vibrating displacement, velocity and acceleration vectors of the structure, respectively; **u** the flow velocity vector (equal to vibrating velocity on the sides of the blade); **p** the pressure vector; **q** the viscous matrix of the flow on the blade sides; **g** the allocated matrix of the pressure on the blade sides; the superscripts '1' and '2' indicate the pressure and suction sides of the blade, respectively; and '0' the interior domain of the structure; for instance, $\mathbf{u}^1 (= \dot{\mathbf{v}}^1)$ represents the velocity vector formed with the node velocity on the pressure side. The derivation of Equation (10) is presented in Appendix A and solved by Wilson-θ method.

3. NUMERICAL METHODS

The problem under consideration includes two phases of the flow and the vibration; thus, it is necessary to simply describe the numerical method for each phase.

3.1. LES of fluid

The finite volume method (FVM) with hybrid discretization schemes of the central difference and the second-order-upwind is employed for the flow with the diffusion and convection terms. Third-order Runge–Kutta algorithm is introduced for time integration in conjunction with a classical

DOI: 10.1002/fld

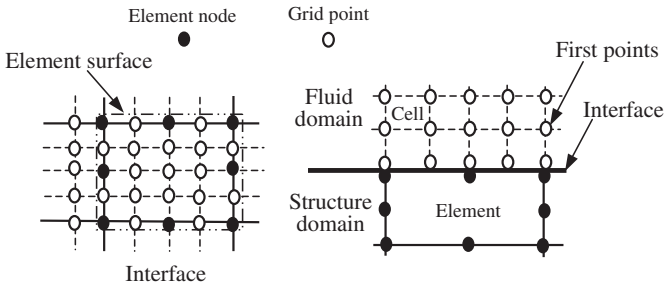

Figure 2. Nodes or points on an interfaced element surface.

correction method at each sub-step. The continuity equation and the pressure gradient terms in the momentum equations are implicitly treated, while the convective and diffusive terms are explicitly treated. The automatic satisfaction of the continuity equation within the computational domain is realized with the SIMPLER algorithm [25]. A strategy of varying the time interval is adopted during the computation to achieve better convergence and accuracy. The maximum time step is limited approximately less than $2.5 \times 10^{-3} T$ (corresponding to $\Delta t \leqslant 0.0004$ s), in which $T = L/U_{\text{ref}} = 0.157$ s is the time of flow passing the blade passage from the inlet to the outlet. The simulating history duration is 1.57 s (approximately $10T$), while the sampling data of the grid turbulence for statistical analysis starts from 0.47 s. Due to using a dynamic SGS model and applying separating iterations for fluid and vibration, respectively, the computational cost is quite high. The typical computational time was successive around 30 days for a simulation time of 1.57 s on a super-workstation with two Intel CPUs of X3.0G.

3.2. *FEM of vibration*

The blade is discretized with 3500 iso-parametric elements attached with 20 nodes and 6 surfaces for conveniently implementing information exchange between flow and vibration. Figure 2 shows the locations of element nodes and grid points on an interfaced element surface. The displacement and velocity at an arbitrary position on the interface are stated as

$$v_i^{\text{fs}}(x, y, z, t) = \sum_{\alpha=1}^{8} N_\alpha(x, y, z) v_{\alpha i}^{\text{fs}}(t) \tag{12}$$

$$\dot{v}_i^{\text{fs}}(x, y, z, t) = u_i^{\text{fs}}(x, y, z, t) = \sum_{\alpha=1}^{8} N_\alpha(x, y, z) \dot{v}_{\alpha i}^{\text{fs}}(t) \tag{13}$$

in which N_α is the interpolation function of the displacement and velocity, α the nodal order on an interfaced element surface, $v_{\alpha i}^{\text{fs}}$ and $\dot{v}_{\alpha i}^{\text{fs}}$ the displacement and velocity at the αth node. Therefore, the velocities at the gird points on the interface are obtained from Equation (13) and are used as vibrating boundary conditions for the simulation of the fluid phase.

The direct integral method based on Wilson-θ scheme [22] is used to solve the vibrating equation of the blade. The discretization schemes on the vibrating velocity and acceleration can be implicitly

DOI: 10.1002/fld

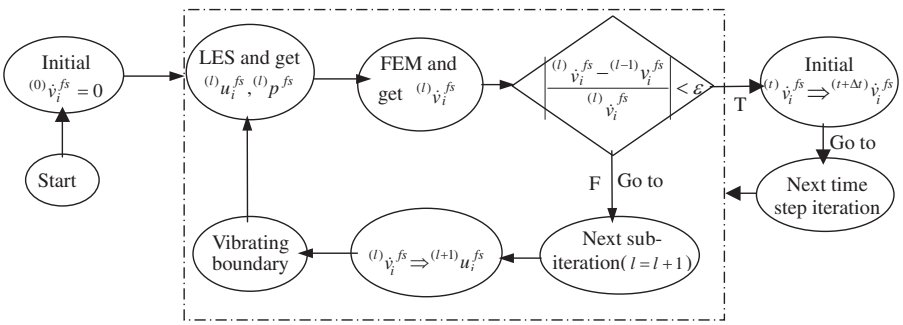

Figure 3. Iteration sketch of whole system.

expressed as

$$\dot{\mathbf{v}}_{t+\theta\Delta t}=\frac{3}{\theta\Delta t}(\mathbf{v}_{t+\theta\Delta t}-\mathbf{v}_t)-2\dot{\mathbf{v}}_t-\frac{\theta\Delta t}{2}\ddot{\mathbf{v}}_t \tag{14}$$

$$\ddot{\mathbf{v}}_{t+\theta\Delta t}=\frac{3}{\theta^2\Delta t^2}(\mathbf{v}_{t+\theta\Delta t}-\mathbf{v}_t)-\frac{6}{\theta\Delta t}\dot{\mathbf{v}}_t-2\ddot{\mathbf{v}}_t \tag{15}$$

in which θ is a parameter related to the numerical stability and taken as 1.4 in this paper, and Δt the time interval, taken as the same as that of fluid phase. The balance equation described by Equation (11) is written as

$$\mathbf{M}\ddot{\mathbf{v}}_{t+\theta\Delta t}+\mathbf{C}\dot{\mathbf{v}}_{t+\theta\Delta t}+\mathbf{K}\mathbf{v}_{t+\theta\Delta t}=\hat{\mathbf{R}}_{t+\theta\Delta t} \tag{16}$$

in which $\hat{\mathbf{R}}_{t+\theta\Delta t}=\mathbf{R}_t+\theta(\mathbf{R}_{t+\Delta t}-\mathbf{R}_t)$. $\mathbf{v}_{t+\theta\Delta t}$ is then obtained by substituting Equations (14) and (15) into Equation (16).

3.3. Numerical iteration

The most suitable methodology for solving the turbulent flow with FSI is probably the direct computing technique based on Equation (A10) in Appendix A, in which the fluid variables (velocity and pressure) and the structure variable (displacement) are simultaneously solved. However, to better utilize the existing computing resources, the iterative method for FSI computation [26] is used to separately solve fluid and structural phases sequentially, albeit more CPU time might be required for repeating some performances of the sub-iterations. The solution iteration sketch of the whole system is shown in Figure 3.

4. NUMERICAL SIMULATION RESULTS

4.1. Pressure characteristics

Figure 4 demonstrates a typical detailed time sequence pressure distributions on both the pressure and suction sides. To investigate the spatial variation of the pressure, we calculated the time-averaged static wall pressure coefficient, $C_{\mathrm{pw}}=2(\overline{p}-\overline{p}_{\mathrm{out}})/U_{\mathrm{ref}}^2$ on both suction and pressure

DOI: 10.1002/fld

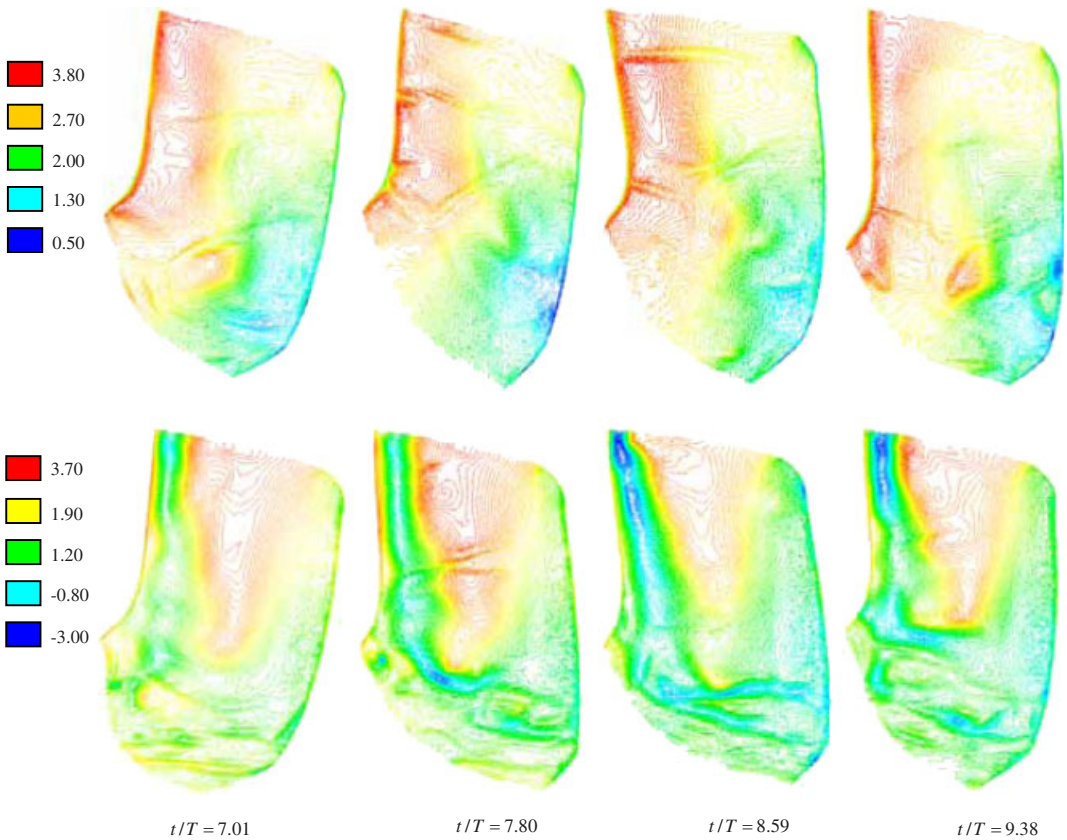

Figure 4. C_{pw} distributions on pressure side (top) and suction side (bottom).

sides of the blade, as shown in Figure 5, where $\overline{p}_{out}$ the mean static pressure in the trailing edge of the blade. For the sake of clarity, only pressure coefficients at three locations, namely top crown (TC), mid position (MP) and bottom ring (BR), are plotted in Figure 5. It is seen from the figure that on the pressure side (designated as PS, solid lines with symbols) of the blade there is a short region of velocity deceleration (corresponding to the increase of pressure) taking place at the leading zone of the blade. Then the velocity starts to accelerate towards the trailing edge at locations of MP and BR. While at location of TC, the situation is different. The pressure remains roughly constant between $x/L = 0.3$ and 0.8 after a short acceleration starts at $x/L = 0.1$. Then a fast acceleration takes place towards the trailing edge of the blade. Figure 5 also demonstrates that at the position of $x/L = 0.1$, the flow has an almost direct impact on the blade, which results in a peak pressure and a low wall-shear stress at three locations of pressure side. Such a low wall-shear stress produces the lowest value of time-averaged skin frictional coefficient (SFC) on the pressure side shown in Figure 6. The distribution of the pressure coefficient on the suction side is different and more complicated than that in the pressure side. An initial drop of the pressure coefficient (corresponding to velocity acceleration) is seen to occur at the leading zone of the blade for three locations selected. Then there is a rapid increase of pressure coefficient (velocity deceleration)

DOI: 10.1002/fld

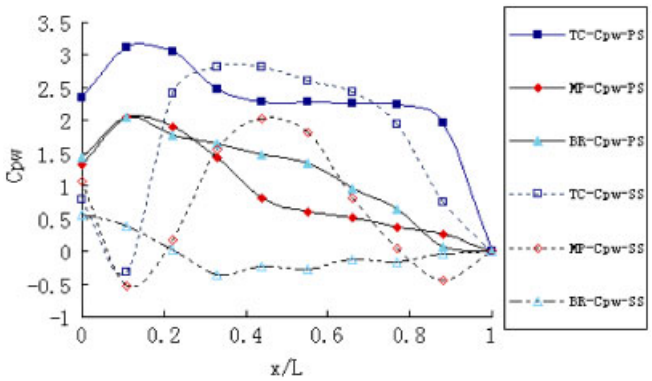

Figure 5. Static pressure coefficient on two wall sides of blade. Keys: PS, pressure side; SS, suction side; TC, crossing line of blade with top crown; MP, mid position line of blade in stream-wise; BR, crossing line of blade with bottom ring; x/L, relative position along each line.

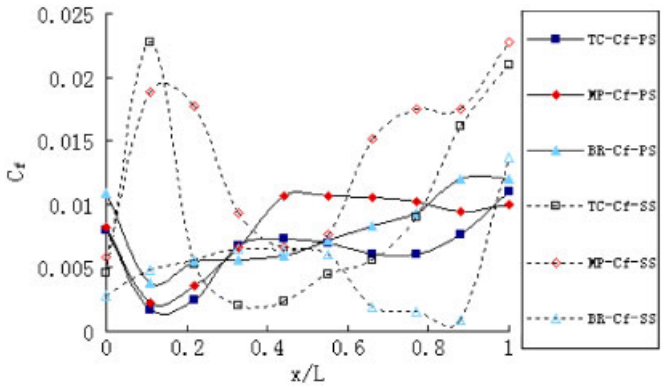

Figure 6. Skin frictional coefficient on two sides of blade. Legends are the same as in Figure 5.

followed by a gradual and then rapid decrease of pressure towards the trailing edge of the blade at locations of TC and MP. A strong vortex is generated at $x/L = 0.1$ which is close to the suction side. As a result, SFC (C_f) increases at this zone, as demonstrated in Figure 6. The pressure coefficient at BR remains roughly constant throughout the passage though there exists a slight decrease at the entrance. It may be worthy of pointing out that the simulated pressure distribution features in this paper are quite different from those in the previous studies [3–6]. Such difference may be mainly ascribed to the different flow configuration treated with the true complex strong 3D turbine passage investigated here.

4.2. Turbulence characteristics

Figure 7 is the instantaneous distributions of the turbulent viscosity at $t/T = 7.01$ and 9.38 for different locations of the passage. It is seen that the turbulent viscosity increases rapidly as the flow passes through the guide vane. The wakes develop towards the downstream and enter the

DOI: 10.1002/fld

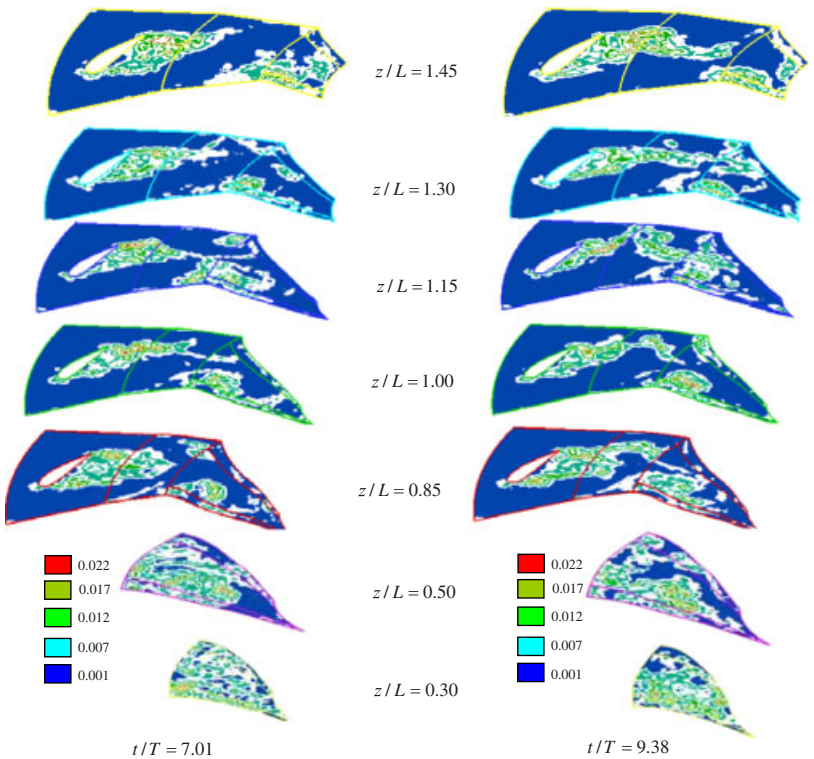

Figure 7. Instantaneous zebras of turbulent viscosity at $t/T = 7.01$ (left column) and 9.38 (right column).

blade passage. A strong turbulence is stirred at the inlet region of the blade passage, particularly at the region close to the suction side. The turbulence is gradually strengthened as the flow approaches the passage bottom. Due to the strong curvature of the blade geometry, the whole passage region is almost filled with the strong turbulence streaks in the region below $z/L = 0.5$. Figure 7 also shows that a strong eddy forms at the inlet region and migrates streamwise on the suction side.

The eddy characteristics are further demonstrated in Figures 8 and 9 of the instantaneous iso-surfaces of vorticity at various time in streamwise and spanwise, respectively. Figure 8 shows the performance of the axial (streamwise) vortex in the blade passage. It is seen that the quantity of these swirls rarefies at the top region of the passage. The distributing law of these swirls looks like a string of green bananas growing in a tree. They are gradually elongated with time and the backbone is finally broken, which makes the bananas fall scatter shortly. As a result, the flow becomes more unstable. In Figure 9, a strong tornado, formed due to influx of two wakes shown in Figure 7 at the leading zones of blade passage, is clearly shown in the leading region near suction side and along the blade height. This large vortex rotates in clockwise direction, and gradually breaks into smaller eddies as it moves into the bottom region of the passage. Consequently, the flow becomes unstable.

DOI: 10.1002/fld

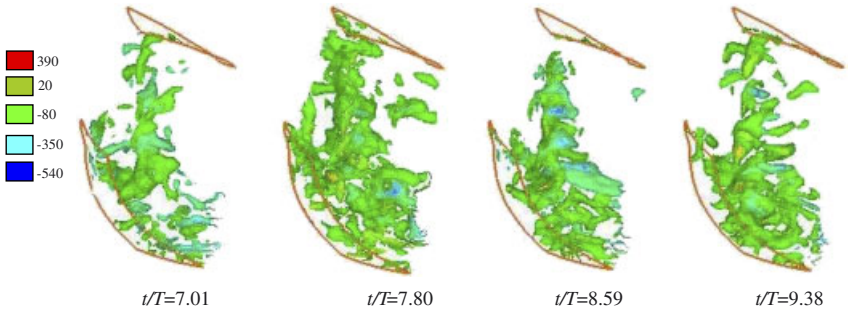

Figure 8. Instantaneous iso-surfaces of stream-wise vorticity at $t/T = 7.01, 7.8, 8.59$ and 9.38.

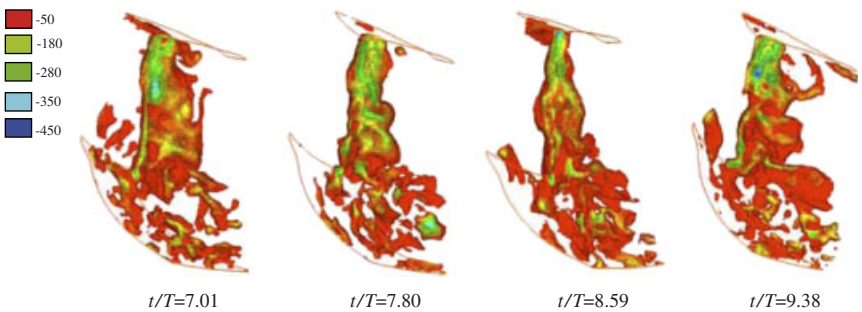

Figure 9. Instantaneous iso-surfaces of span-wise vorticity at $t/T = 7.01, 7.8, 8.59$ and 9.38.

4.3. Flow structures near walls

To investigate the features of the flow structures on vibration walls, two surfaces near the pressure and suction sides are selected, respectively, by rotation of 0.4°, approximately 1.6 mm (about $y^+ = 70$) away from the walls (maximum vibration magnitude of the blade is about 1.6 mm for this case) at the crossing edge with the bottom ring. These two surfaces are referred to as S2 and S4. Figures 10 and 11 are the typical example of the axial and span-wise vortexes on S2 and S4, respectively.

Figure 10(a) shows an order distribution of longitudinal vortex on S2, especially at the bottom region (near BR). At this region, the vibration is weaker and the curvature change of the blade is more uniform. Therefore, the vortexes generated are comparatively longitudinal, which are similar to those found in [3]. The influence of the vibration on the flow structures is evidenced by looking at the mid-top region of S2, where the longitudinal vortexes become shorter and much scattered. The distributions of the span-wise vortexes on S2 seem to be more complicated (see Figure 11(a)). In general, a blurry order of the vortexes takes place due to non-uniform flow direction adjustment along the blade height, which coincides with the flow nature in the blade passage of a Francis turbine. The distributions of the vortexes on the suction side (S4) shown in Figures 10(b) and 11(b) are very different due to a protruding blade wall surface. In general, the simulation results reveal that the effects of the blade vibration on the near wall flow structure on S4 are smaller than that on S2.

DOI: 10.1002/fld

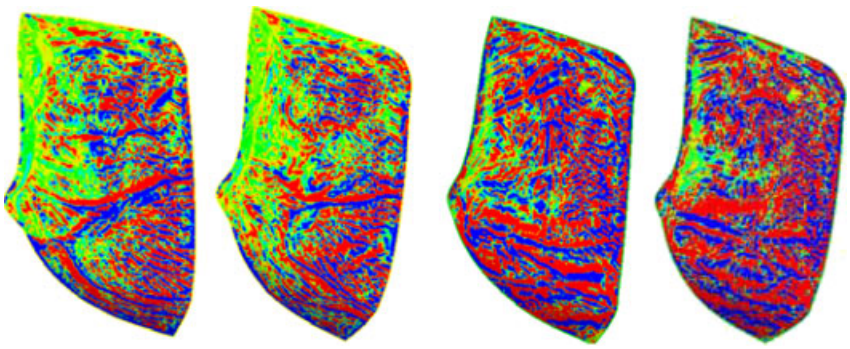

Figure 10. Axial vorticity distributions near pressure and suction sides (S2 and S4 surfaces) at $t/T = 7.01$ and 9.38: (a) pressure side; and (b) suction side.

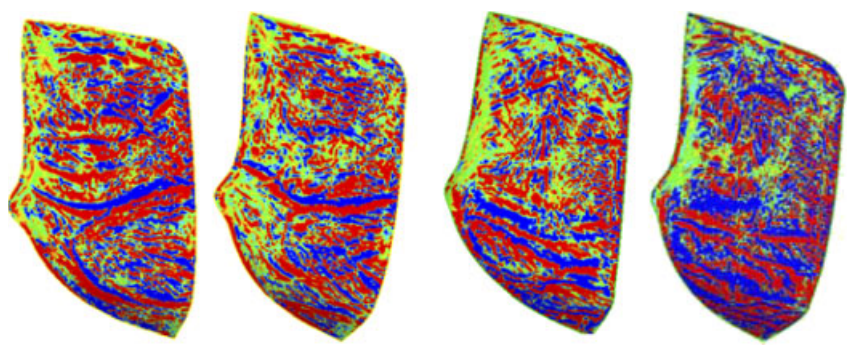

Figure 11. Span-wise vorticity distributions near pressure and suction sides (S2 and S4 surfaces) at $t/T = 7.01$ and 9.38: (a) pressure side; and (b) suction side.

Figure 12 is the distribution of the turbulent spots on the surface of $y^+ \approx 6$ (approximately 0.2 mm) away from the blade wall at $t/T = 5.044$. It is seen that the turbulent spots are mixed with some regulative contours. This phenomenon indicates that the flow is in a transitional state. On the near-pressure side surface, the turbulent spots distribute mainly in a belt form from the top-left to the bottom-right zones, while a scatter U-shaped type of the turbulent spots is found on the near-suction side surface. Such distributions are quite different in rigid walls as found by Zhang *et al*. [27], which reflects the different energy-transfer mechanism near the walls due to the vibration.

DOI: 10.1002/fld

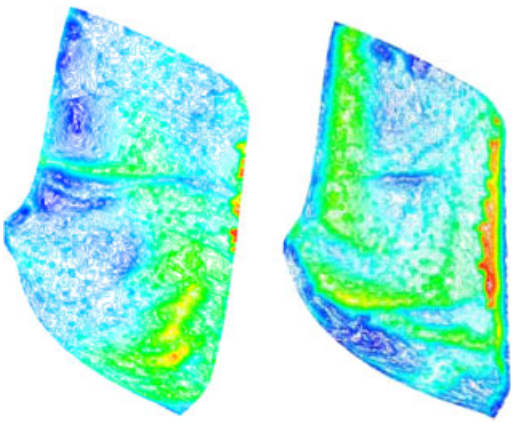

(a) (b)

Figure 12. Distributions of turbulent spots at $t/T = 5.044$: (a) on $y^+ \approx 6$ surface of pressure side; and (b) on $y^+ \approx 6$ surface of suction side.

(a) (b)

Figure 13. Main components of test model: (a) model runner; and (b) model unit.

5. EXPERIMENTS AND COMPARISON

5.1. Experimental rigs

The turbine used for the experiments is a model of a Francis turbine, A55x. The model runner diameter is 450 mm, with 10 blades and, 23 guide vanes and 23 stay vanes. The model material is hard polyglass with Young's modulus of 2500 MPa, Poisson ratio of 0.384, and the mass density of 1280 kg/m^3. The maximum net working water head in the experiments is 3.28 m. The rotation velocity varies from zero to 210 r/min according to the needs. Figure 13 is the photo of the experimental facility.

Five pressure sensors, LL-072-25A, were mounted on both the pressure side (numbered 47–51) and the suction side (numbered 52–56) of a blade to record the turbulent pressure signal. The

DOI: 10.1002/fld

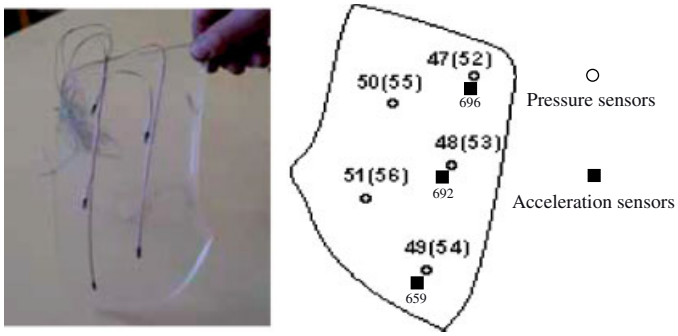

Figure 14. Transducer positions mounted on blade.

locations of the sensors are shown in Figure 14 in which the pressure sensors were arranged in a way that they (from 50(55) to 48(53) and from 51(56) to 49(54)) were roughly placed along the stream-wise direction. Three acceleration transducers, numbered 659, 692 and 696, were installed inside another blade (unfortunately transducer 696 did not work during the experiments). The sampling resolutions are 2.5, 5, 7.5 and 10 kHz for flow, and 0.5, 1, 2.5 and 5 kHz for vibration, respectively.

5.2. Comparison

The experimental parameters are the same as that of the numerical example, namely the working net water head is 3.28 m, the opening of the guide vanes is 22 mm, and the averaged velocity on the inlet section of the blade passage is 1 m/s. The data used in present study are of sampling resolutions of 2.5 kHz.

Figure 15 is the comparison of the simulated (solid squares) and measured (solid triangles) time-averaged total pressures (static plus dynamic pressures) at the specified points. In general, the simulated time-averaged pressures agree well with the measurements with the maximum relative error being about 9% (at suction side point 54). The results show that the pressure on the pressure side decreases rapidly along the stream-wise direction (from 50 to 48 and from 51 to 49), while on the suction side, the pressure drop becomes more gradual (see dotted arrow lines in Figure 15). Such features of the pressure distribution are consistent with those shown in Figures 5 and 6.

Figure 16 is the simulated (solid line) and measured (dotted line) time-dependent pressures at the measuremental points in which the signals were treated with five wavelet decompositions of the DB4 wavelet function in order to obtain smooth curves for the purpose of comparison. The figure demonstrates much information of flow. Let us first look at the pressure histories at the upper region of the blade (i.e. points 47, 50 and 52, 55), in which the thickness of the blade is bigger and the vibration is naturally weaker. It is seen that (i) there are only several peaks and troughs over the recorded time interval; and (ii) the variation range of the pressure is relatively small compared to that in the lower zone of the blade. This implies that the flow turbulence is weaker at the upper region and the influence of the structure vibration on the near-wall flow is weaker. The situation of the pressure history at the lower region of the blade is contrary. The thinner blade results in a significant vibration, which makes the pressure history become more complicated. It is seen that

DOI: 10.1002/fld

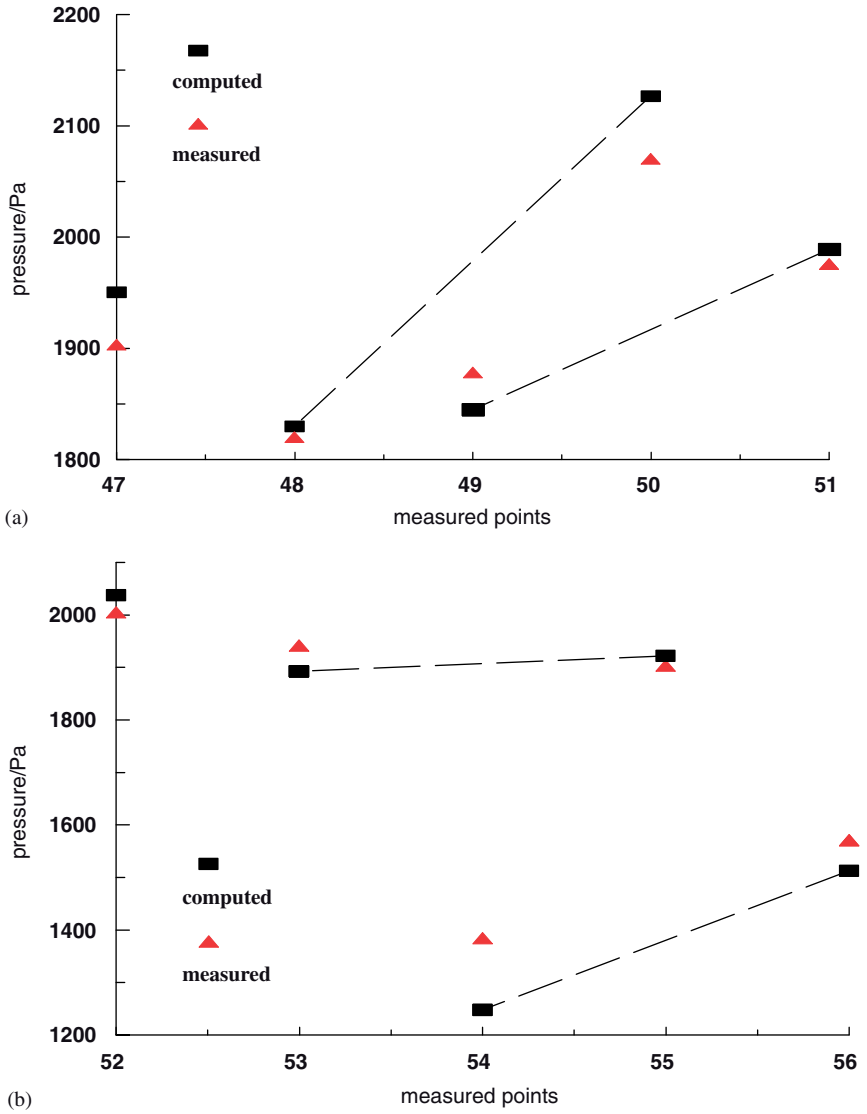

Figure 15. Comparisons of computational and measured pressures: (a) on pressure side; and (b) on suction side.

many pressure peaks and troughs take place and the pressure variation range is much wider. Such features may be ascribed to the presence of the dominant small-scale components of the turbulent flow in this region.

Figure 17 is a tendency comparison of the computed (solid line) and measured (dotted line) accelerations of the blade. In general, the features of the simulated and measured acceleration history are similar to that of the pressure histories. The results show that the acceleration histories

DOI: 10.1002/fld

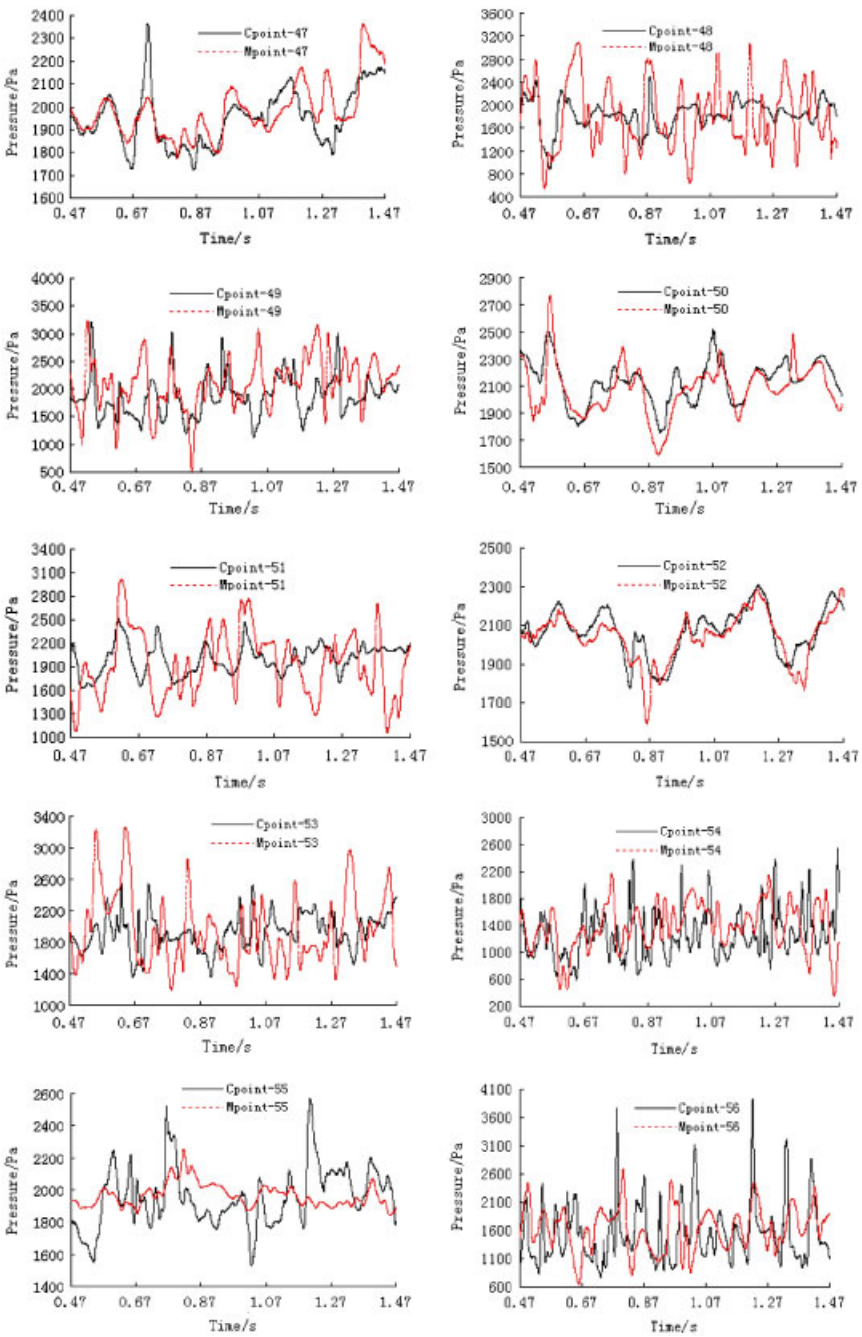

Figure 16. History comparisons of total pressure at measured points on two sides.

DOI: 10.1002/fld

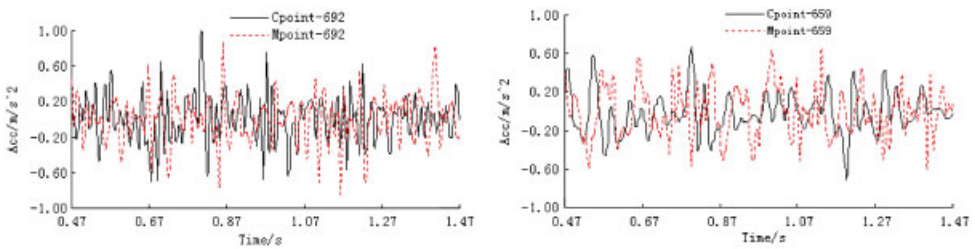

Figure 17. Vibration accelerations of blade at specified points.

at two points are quite different in details. The vibration at the midst of the blade (Accelerator-692) is faster than that at the bottom of the blade (Accelerator-659). This implies that the dominant frequencies of governing the vibration features of the blade have the spatial variation characteristics. The vibration is strongly performed in a localization flutters [20].

6. CONCLUSIONS

LES has been performed with a one-coefficient dynamic SGS model and consideration of a dynamically FSI to investigate the turbulent flow with high Reynolds number in a strong 3D complex passage of a true Francis turbine. The results show that the influences of FSI on the distribution and development of the near-wall flow structures are strong. The energy-transfer mechanism between the large and small scales is disturbed by the vibration. The temporal and spatial distribution of the turbulent flow in the blade passage is non-uniform. For example, the TKE in the top region of the passage is very small with a value of about 1.5% of the mean flow, while at the bottom and trailing regions, the TKE is significantly enhanced and reaches about 50% near the suction side. Such feature may be ascribed to the stirring of the blade vibration and strong curvature variation of the blade wall surfaces.

Results also demonstrate that large attack angle due to small opening of the guide vane causes strong wakes at the inlet. The wakes are the main reason for forming the primary vortex in the leading region of the passage. As the primary vortex evolves along the suction side near the blade, it is broken into smaller vortex due to strong curvature and the vibration of the blade, which causes the continuous elongation of the tube vortex and rapidly breaks down into many tiny vortexes.

APPENDIX A

The computational sub-domain concerning only blade passage consisting of two blades and fluid between these blades is shown in Figure A1, in which the fluid domain, Ω^{f}, is surrounded by surfaces $\Gamma^{\mathrm{f}} = A1 + A2 + A3 + A4 + A5 + A6$, and the structural domain, Ω^{s}, is formed by surfaces $\Gamma^{\mathrm{s}} = A3 + A4 + A7 + A8$.

DOI: 10.1002/fld

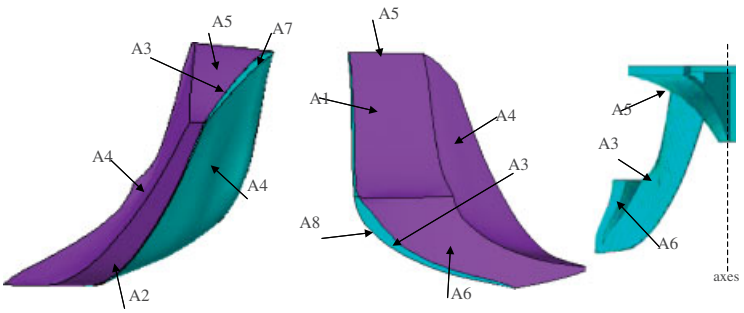

Figure A1. Computational domain of blade passage.

Neglecting the viscous damping of the structure material, then the governing equations for the blade are stated as

$$\sigma^{\mathrm{s}}_{ij,j} + F^{\mathrm{s}}_i - \rho^{\mathrm{s}}\ddot{v}_i = 0 \quad \text{in } \Omega^{\mathrm{s}} \tag{A1a}$$

$$\varepsilon^{\mathrm{s}}_{ij} = \tfrac{1}{2}(v_{i,j} + v_{j,i}) \quad \text{in } \Omega^{\mathrm{s}} \tag{A1b}$$

$$\sigma^{\mathrm{s}}_{ij} = \lambda\varepsilon^{\mathrm{s}}_{kk}\delta_{ij} + 2G\varepsilon^{\mathrm{s}}_{ij} \quad \text{in } \Omega^{\mathrm{s}} \tag{A1c}$$

$$v_i = 0 \quad \text{on surfaces } A7 \text{ and } A8 \tag{A2}$$

For incompressible viscous fluid, the governing equations are written as

$$\frac{\partial u_i}{\partial t} + u_j u_{i,j} - \sigma^{\mathrm{f}}_{ij,j} - F^{\mathrm{f}}_i = 0 \quad \text{in } \Omega^{\mathrm{f}} \tag{A3a}$$

$$u_{k,k} = 0 \quad \text{in } \Omega^{\mathrm{f}} \tag{A3b}$$

$$\sigma^{\mathrm{f}}_{ij} = -p\delta_{ij} + \nu(u_{i,j} + u_{j,i}) = -p\delta_{ij} + 2\nu S_{ij} \quad \text{in } \Omega^{\mathrm{f}} \tag{A3c}$$

$$u_i = u_{0i} \quad \text{on surfaces } A1 \text{ and } A2 \tag{A4}$$

At the interfaces between the fluid and the structure, the compatible coupling conditions are

$$u^{\mathrm{fs}}_i - \dot{v}^{\mathrm{fs}}_i = 0 \quad \text{on surfaces } A3\text{–}A6 \tag{A5a}$$

$$\sigma^{\mathrm{f}}_{ij} n^{\mathrm{f}}_j + \sigma^{\mathrm{s}}_{ij} n^{\mathrm{s}}_j = 0 \quad \text{on surfaces } A3\text{–}A6 \tag{A5b}$$

where σ^{s}_{ij} is the stress tensor of the structure, $\varepsilon^{\mathrm{s}}_{ij}$ the strain tensor, F^{s}_i the body forces acting on the structure, ρ_{s} the mass density of the structural material, n_j the unit outer normal direction on the interface, σ^{f}_{ij} the viscous stress tenors of the fluid, S_{ij} the strain rate tensor, for the rest of the variables please refer to Section 2.

According to the maximum dissipative power principle for fluid flow on the Garlerkin method [28] and application of 4 types of Lagrangian multipliers, γ, β_i, π_i and λ_i which correspond to restricted conditions of Equations (A3b), (A2), (A4) and (A5a), a power functional of the FSI system is constructed and its variation with respect to the basic variables $(u_i, p, \dot{v}_i)$ and the

DOI: 10.1002/fld

Lagrangian multipliers is obtained as

$$\begin{aligned}\delta\Pi^{\mathrm{FSI}} = &\iiint_{\Omega^{\mathrm{f}}}[\dot{u}_i + u_j u_{i,j} - F_i^{\mathrm{f}} - \nu(u_{i,j} + u_{j,i})_{,j} - \gamma_{,i}]\delta u_i \,\mathrm{d}\Omega \\ &+ \iiint_{\Omega^{\mathrm{f}}} u_{i,i}\delta\gamma \,\mathrm{d}\Omega + \iiint_{\Omega^{\mathrm{s}}}(\rho^{\mathrm{s}}\ddot{v}_i - \sigma^{\mathrm{s}}_{ij,j} - \rho^{\mathrm{s}}F_i^{\mathrm{s}})\delta\dot{v}_i \,\mathrm{d}\Omega \\ &+ \iint_{A7+A8}[\delta\beta_i\dot{v}_i + (\beta_i + \sigma^{\mathrm{s}}_{ij}n^{\mathrm{s}}_j)\delta\dot{v}_i]\,\mathrm{d}A \\ &+ \iint_{A1+A2}[\delta\pi_i(u_i^{\mathrm{f}} - u_{0i}) + [\pi_i + \nu(u_{i,j} + u_{j,i})n^{\mathrm{f}}_j + \gamma\delta_{ij}n^{\mathrm{f}}_j]\delta u_i]\,\mathrm{d}A \\ &+ \iint_{A3+A4+A5+A6}(\sigma^{\mathrm{s}}_{ij}n^{\mathrm{s}}_j - \lambda_i)\delta\dot{v}_i^{\mathrm{fs}}\,\mathrm{d}A \\ &+ \iint_{A3+A4+A5+A6}[\nu(u^{\mathrm{fs}}_{i,j} + u^{\mathrm{fs}}_{j,i})n^{\mathrm{f}}_j + \gamma\delta_{ij}n^{\mathrm{f}}_j + \lambda_i]\delta u_i^{\mathrm{fs}}\,\mathrm{d}A \\ &+ \iint_{A3+A4+A5+A6}\delta\lambda_i(u_i^{\mathrm{fs}} - \dot{v}_i^{\mathrm{fs}})\,\mathrm{d}A \end{aligned} \tag{A6}$$

The Lagrangian multipliers, which meet the variational stationary condition, $\delta\Pi^{\mathrm{FSI}} = 0$, are solved as

$$\gamma = -p \tag{A7a}$$

$$\beta_i = -\sigma^{\mathrm{s}}_{ij}n^{\mathrm{s}}_j \tag{A7b}$$

$$\pi_i = -\sigma^{\mathrm{f}}_{ij}n^{\mathrm{f}}_j \tag{A7c}$$

$$\lambda_i = (\sigma^{\mathrm{s}}_{ij}n^{\mathrm{s}}_j - \sigma^{\mathrm{f}}_{ij}n^{\mathrm{f}}_j)/2 \tag{A7d}$$

It is easy to get the foregoing governing equations of both the structure and the fluid by Equation (A6) and the Lagrangian multipliers solved. Thus, the functional of the FSI system is

$$\Pi^{\mathrm{FSI}} = \hat{\Pi}_0^{\mathrm{f}} + \hat{\Pi}_0^{\mathrm{s}} + \Pi_1^{\mathrm{f}} + \Pi_1^{\mathrm{s}} + \Pi^{\mathrm{fs}} \tag{A8a}$$

in which,

$$\delta\hat{\Pi}_0^{\mathrm{f}} = \iiint_{\Omega^{\mathrm{f}}}(\dot{u}_i + u_j u_{i,j})\delta u_i \,\mathrm{d}\Omega \tag{A8b}$$

$$\delta\hat{\Pi}_0^{\mathrm{s}} = \frac{1}{2}\iiint_{\Omega^{\mathrm{s}}}\sigma^{\mathrm{s}}_{ij}\delta\dot{v}_{i,j}\,\mathrm{d}\Omega + \iiint_{\Omega^{\mathrm{s}}}\rho^{\mathrm{s}}\ddot{v}_i\delta\dot{v}_i\,\mathrm{d}\Omega \tag{A8c}$$

$$\Pi_1^{\mathrm{f}} = -\iiint_{\Omega^{\mathrm{f}}}\left[F_i^{\mathrm{f}}u_i - \frac{1}{2}\nu(u_{i,j} + u_{j,i})u_{i,j} + pu_{i,i}\right]\mathrm{d}\Omega - \iint_{A1+A2}\sigma^{\mathrm{f}}_{ij}n^{\mathrm{f}}_j(u_i - u_{0i})\,\mathrm{d}A \tag{A8d}$$

DOI: 10.1002/fld

$$\Pi_1^{\mathrm{s}} = -\iiint_{\Omega^{\mathrm{s}}} \rho^{\mathrm{s}} F_i^{\mathrm{s}} \dot{v}_i \, \mathrm{d}\Omega - \iint_{A7+A8} \sigma_{ij}^{\mathrm{s}} n_j^{\mathrm{s}} \dot{v}_i \, \mathrm{d}A \tag{A8e}$$

$$\Pi^{\mathrm{fs}} = \iint_{A3+A4+A5+A6} \frac{1}{2}(\sigma_{ij}^{\mathrm{s}} n_j^{\mathrm{s}} - \sigma_{ij}^{\mathrm{f}} n_j^{\mathrm{f}})(u_i^{\mathrm{fs}} - \dot{v}_i^{\mathrm{fs}}) \, \mathrm{d}A \tag{A8f}$$

where Equations (A8b) and (A8c) appear in the variational form (with symbol 'δ'). It is easy to prove that the solution, $[u_i, p, \dot{v}_i]$, which satisfies the functional equations (A8), is that of the FSI system in this study.

To get a discretization scheme of the FEM for the structure, interpolation functions are applied to Equations (A8), namely, the displacement (for structure) and the velocity and the pressure (for fluid) at arbitrary point in an element (for fluid and structure) are expressed with the values at the nodes of this element

$$v_i^e(x, y, x, t) = N_\alpha^{\mathrm{s}}(x, y, x) v_{\alpha i}^e(t) \tag{A9a}$$

$$u_i^e(x, y, x, t) = N_\alpha^{\mathrm{f}}(x, y, x) u_{\alpha i}^e(t) \tag{A9b}$$

$$p^e(x, y, x, t) = N_\alpha^{\mathrm{p}}(x, y, x) p_\alpha^e(t) \tag{A9c}$$

in which, α indicates the nodal order of element, N_α^{s} is the displacement interpolation function for the structure, N_α^{f} and N_α^{p}, respectively, the velocity and pressure interpolation functions for the fluid. Introducing Equation (A9) into Equation (A8) and making a lengthy variational operation with respect to the variables $[u_i, p, \dot{v}_i]$, the fully coupled FEM equation for the FSI system are obtained as (for eth element for structural- or fluid-domain)

$$\mathbf{m}_e^{\mathrm{f}} \dot{\mathbf{u}}_e + \mathbf{c}_e^{\mathrm{f}} \mathbf{u}_e + \mathbf{g}_e^{\mathrm{f}} \mathbf{p}_e + \mathbf{q}_e^{\mathrm{fs}} \dot{\mathbf{v}}_e + \mathbf{k}_e^{\mathrm{f}} \mathbf{v}_e + \mathbf{r}_e^{\mathrm{f}} = 0 \tag{A10a}$$

$$\mathbf{m}_e^{\mathrm{s}} \ddot{\mathbf{v}}_e^{\mathrm{s}} + \mathbf{k}_e^{\mathrm{s}} \mathbf{v}_e + \mathbf{q}_e^{\mathrm{fs}} \mathbf{u}_e + \mathbf{g}_e^{\mathrm{s}} \mathbf{p}_e + \mathbf{r}_e^{\mathrm{s}} = 0 \tag{A10b}$$

$$\mathbf{g}_e^{\mathrm{f}} \mathbf{u}_e + \mathbf{g}_e^{\mathrm{s}} \dot{\mathbf{v}}_e + \mathbf{r}_e^{\mathrm{p}} = 0 \tag{A10c}$$

in which, $\mathbf{v}_e$, $\mathbf{u}_e$ and $\mathbf{p}_e$ are the nodal vectors of the structural displacement, the flow velocity and the pressure. The rest of the symbols are

$$\mathbf{m}_e^{\mathrm{f}} = \iiint_{\Omega^{\mathrm{f}}} \breve{\mathbf{N}}^{\mathrm{f}} \mathbf{N}^{\mathrm{f}} \, \mathrm{d}\Omega, \quad \mathbf{m}_e^{\mathrm{s}} = \iiint_{\Omega^{\mathrm{s}}} \rho^{\mathrm{s}} \breve{\mathbf{N}}^{\mathrm{s}} \mathbf{N}^{\mathrm{s}} \, \mathrm{d}\Omega$$

$$\mathbf{c}_e^{\mathrm{f}} = \iiint_{\Omega^{\mathrm{f}}} [\breve{\mathbf{N}}^{\mathrm{f}} \mathbf{N}^{\mathrm{f}} \mathbf{u}_e \partial \mathbf{N}^{\mathrm{f}} - 2\nu \breve{\mathbf{N}}^{\mathrm{f}} \mathbf{J} \breve{\mathbf{J}}^{\mathrm{f}}] \, \mathrm{d}\Omega + 4\nu \iint_{A1+A2} \breve{\mathbf{N}}^{\mathrm{f}} \mathbf{n} \breve{\mathbf{J}} \mathbf{N}^{\mathrm{f}} \, \mathrm{d}A$$
$$- 2\nu \iint_{A3+A4+A5+A6} \breve{\mathbf{N}}^{\mathrm{f}} \mathbf{n} \breve{\mathbf{J}} \mathbf{N}^{\mathrm{f}} \, \mathrm{d}A$$

$$\mathbf{q}_e^{\mathrm{fs}} = \nu \iint_{A3+A4+A5+A6} \breve{\mathbf{N}}^{\mathrm{f}} \mathbf{n} \breve{\mathbf{J}} \mathbf{N}^{\mathrm{s}} \, \mathrm{d}A$$

$$\mathbf{g}_e^{\mathrm{f}} = \iiint_{\Omega^{\mathrm{f}}} \breve{\mathbf{N}}^{\mathrm{f}} \breve{\partial} \mathbf{N}^{\mathrm{p}} \, \mathrm{d}\Omega - \iint_{A1+A2} \breve{\mathbf{N}}^{\mathrm{f}} \mathbf{n} \boldsymbol{\delta} \mathbf{N}^{\mathrm{p}} \, \mathrm{d}A$$

DOI: 10.1002/fld

$$+\frac{1}{2}\iint_{A3+A4+A5+A6}\breve{\mathbf{N}}^{\mathrm{f}}\mathbf{n}\delta\mathbf{N}^{\mathrm{p}}\,\mathrm{d}A$$

$$\mathbf{r}_e^{\mathrm{f}}=\iiint_{\Omega^{\mathrm{f}}}\breve{\mathbf{N}}^{\mathrm{f}}\mathbf{N}^{\mathrm{f}}\mathbf{F}_e^{\mathrm{f}}\,\mathrm{d}\Omega-2\nu\iint_{A1+A2}\breve{\mathbf{N}}^{\mathrm{f}}\mathbf{n}\breve{\mathbf{J}}\,\mathbf{N}^{\mathrm{f}}\mathbf{u}_{0e}\,\mathrm{d}A$$

$$\mathbf{g}_e^{\mathrm{s}}=-\frac{1}{2}\iint_{A3+A4+A5+A6}\breve{\mathbf{N}}^{\mathrm{s}}\mathbf{n}\delta\mathbf{N}^{\mathrm{p}}\,\mathrm{d}A,\quad \mathbf{r}_e^{\mathrm{s}}=-\iiint_{\Omega^{\mathrm{s}}}\rho^{\mathrm{s}}\breve{\mathbf{N}}^{\mathrm{s}}\mathbf{N}^{\mathrm{s}}\mathbf{F}_e^{\mathrm{s}}\,\mathrm{d}\Omega$$

$$\mathbf{r}_e^{\mathrm{p}}=\iint_{A1+A2}\breve{\mathbf{N}}^{\mathrm{f}}\mathbf{n}\delta\mathbf{N}^{\mathrm{p}}\mathbf{u}_{0e}\,\mathrm{d}A$$

$$\mathbf{k}_e^{\mathrm{f}}=\frac{1}{2}\iint_{A3+A4+A5+A6}\breve{\mathbf{N}}^{\mathrm{s}}\mathbf{n}\mathbf{D}\mathbf{C}\mathbf{N}^{\mathrm{f}}\,\mathrm{d}A$$

$$\mathbf{k}_e^{\mathrm{s}}=\iiint_{\Omega^{\mathrm{s}}}\breve{\mathbf{N}}^{\mathrm{s}}\mathbf{J}\mathbf{D}\mathbf{C}\mathbf{N}^{\mathrm{s}}\,\mathrm{d}\Omega-\iint_{A7+A8}\breve{\mathbf{N}}^{\mathrm{s}}\mathbf{n}\mathbf{D}\mathbf{C}\mathbf{N}^{\mathrm{s}}\,\mathrm{d}A-\frac{1}{2}\iint_{A3+A4+A5+A6}\breve{\mathbf{N}}^{\mathrm{s}}\mathbf{n}\mathbf{D}\mathbf{C}\mathbf{N}^{\mathrm{f}}\,\mathrm{d}A$$

$$\mathbf{C}=\begin{bmatrix}\dfrac{\partial}{\partial x_1} & 0 & 0 & \dfrac{1}{2}\dfrac{\partial}{\partial x_2} & 0 & \dfrac{1}{2}\dfrac{\partial}{\partial x_3}\\ 0 & \dfrac{\partial}{\partial x_2} & 0 & \dfrac{1}{2}\dfrac{\partial}{\partial x_1} & \dfrac{1}{2}\dfrac{\partial}{\partial x_3} & 0\\ 0 & 0 & \dfrac{\partial}{\partial x_3} & 0 & \dfrac{1}{2}\dfrac{\partial}{\partial x_2} & \dfrac{1}{2}\dfrac{\partial}{\partial x_1}\end{bmatrix}$$

$$\mathbf{J}=\begin{bmatrix}\dfrac{\partial}{\partial x_1} & 0 & 0 & \dfrac{\partial}{\partial x_2} & 0 & \dfrac{\partial}{\partial x_3}\\ 0 & \dfrac{\partial}{\partial x_2} & 0 & \dfrac{\partial}{\partial x_1} & \dfrac{\partial}{\partial x_3} & 0\\ 0 & 0 & \dfrac{\partial}{\partial x_3} & 0 & \dfrac{\partial}{\partial x_2} & \dfrac{\partial}{\partial x_1}\end{bmatrix}$$

$$\mathbf{n}=\begin{bmatrix}n_1 & 0 & 0 & n_2 & 0 & n_3\\ 0 & n_2 & 0 & n_1 & n_3 & 0\\ 0 & 0 & n_3 & 0 & n_2 & n_1\end{bmatrix},\quad \boldsymbol{\delta}=[1\ \ 1\ \ 1\ \ 0\ \ 0\ \ 0]^{\mathrm{T}},\quad \partial=[\partial/\partial x_1\ \ \partial/\partial x_2\ \ \partial/\partial x_3]$$

D is the elastic matrix of the structure, **N** the interpolation function matrix, $\breve{\mathbf{N}}$ the transformation of matrix **N**, and $\breve{\mathbf{J}}$ the transformation of matrix **J**. Thus, Equation (13) can be obtained by equating Equations (A10) into the global equation and neglecting the body force of the structure (i.e. $\mathbf{r}^{\mathrm{s}}=\mathbf{0}$). (Note: $A5$ and $A6$ are considered as rigid surfaces in the present study.)

DOI: 10.1002/fld

NOMENCLATURE

A	area
C_{pw}	pressure coefficient on wall
G	material constant of blade
L	length of geometry size
N_α	interpolating function
T	defined as L/U_{ref}
U_{ref}	mean flow velocity at the inlet
T_{ij}	subtest stresses
S_{ij}	strain for fluid
c_{d}	coefficient of the dynamical SGS model
n_j	unit outer normal direction
p	pressure divided by the fluid mass density
p_{out}	pressure at the outlet
$\overline{p}$	filtered pressure divided by mass density
r	rotating radius to x_3-axes
t	time
Δt	time interval
u_i	component of flow velocity
$\dot{u}_i$	$=\partial u_i/\partial t$
$\overline{u}_i$	filtered component of flow velocity
$\overline{\overline{u}}_i$	test filtered component of flow velocity
v_i	component of displacement of vibration
$\dot{v}_i$	component of velocity of the vibration
$\ddot{v}_i$	component of acceleration of the vibration
x_i	co-ordinate component of Cartesian system
x, y, z	co-ordinate component of Cartesian system
y^+	defined as $y^+=(\Delta y/\nu)\sqrt{\tau_{\mathrm{w}}/\rho_{\mathrm{f}}}$
Δx_i	space of grid pint
$\overline{\overline{G}}$	test filter
$\overline{\overline{\Delta}}$	characteristic width of the test filter
$\overline{\Delta}$	characteristic width of the filter
Ω^{f}	fluid domain
Ω^{s}	solid domain
Π	functional
σ^{f}_{ij}	stresses in fluid
σ^{s}_{ij}	stresses in blade
ε_{i3k}	circular replacement tensor
τ_{ij}	SGS stresses
$\overline{\overline{\tau}}_{ij}$	SGS stresses on the test filter
$\varepsilon^{\mathrm{s}}_{ij}$	strain rate for solid
δ_{ij}	Kronecker's delta
ν	kinetic viscosity of fluid
ν_T	eddy viscosity of fluid

DOI: 10.1002/fld

ω	rotating angular velocity
λ	material constant for blade
λ_i	Lagrangian multiplier
π_i	Lagrangian multiplier
β_i	Lagrangian multiplier
γ	Lagrangian multiplier
$\delta(\cdot)$	variational symbol
ρ^s	liquid mass density
$\langle\,\rangle$	ensemble averaging operation

Matrices

$\mathbf{M}$	mass matrix
$\mathbf{C}$	damping matrix
$\mathbf{K}$	stiffness matrix
$\mathbf{D}$	elastic matrix of blade
$\mathbf{R}$	blade excitation vector caused by flow
$\mathbf{v}$, $\dot{\mathbf{v}}$, $\ddot{\mathbf{v}}$	vectors of displacement, velocity, and acceleration for the blade
$\mathbf{u}$	vector of velocity for the fluid

Superscripts or subscripts

f	fluid
s	structure (blade)
fs	interface of fluid and structure
α	node order of element for FEM

ACKNOWLEDGEMENTS

The authors thank the National Natural Science Foundation of China (NSFC) (Grant no. 90210005 and 50579025) for financial support of this research. The comments made by two anonymous reviewers greatly improved the quality of the paper.

REFERENCES

1. Lai XD. Analysis and estimation of hydraulic stability of Francis hydro turbine. *Journal of Hydrodynamics*, *Series B* 2004; **16**(2):194–200.
2. Xin Z, Zhang LJ, Chang JS. Numerical simulation of three-dimensional turbulent flow through a turbine spiral casing with stay ring and guide vanes. *Journal of Hydrodynamics*, *Series A* 2004; **19**(6):713–718.
3. Wu XH, Durbin PA. Evidence of longitudinal vortices evolved from distorted wakes in a turbine passage. *Journal of Fluid Mechanics* 2001; **446**:199–228.
4. Kalitzin G, Wu XH, Durbin PA. DNS of fully turbulent flow in a LPT passage. *International Journal of Heat and Fluid Flow* 2003; **24**:636–644.
5. Wissink JG. DNS of separating, low Reynolds number flow in a turbine cascade with incoming wakes. *International Journal of Heat and Fluid Flow* 2003; **24**:626–635.
6. Rodi W. DNS and LES of some engineering flows. *Fluid Dynamics Research* 2006; **38**:145–173.
7. Moin P, Mahesh K. Direct numerical simulation: a tool in turbulence research. *Annual Review of Fluid Mechanics* 1998; **30**:539–578.

DOI: 10.1002/fld

8. Jordan SA. A large-eddy simulation methodology in generalized curvilinear coordinates. *Journal of Computational Physics* 1999; **148**:322–340.
9. Mahesh K, Constantinescu GS, Moin P. Large-eddy simulation of gas-turbine combustors. *CTR Annual Research Briefs*. NASA Ames/Stanford University, 2000.
10. Morinishi Y, Lund TS, Vasilyev OV, Moin P. Fully conservative higher order finite difference schemes for incompressible flow. *Journal of Computational Physics* 1998; **143**:90–124.
11. Moin P. Advances in large eddy simulation methodology for complex flows. *International Journal of Heat and Fluid Flow* 2002; **24**:710–720.
12. Conway S, Caraeni D, Fuchs L. Large eddy simulation of the flow through the blades of a swirl generator. *International Journal of Heat and Fluid Flow* 2002; **21**:664–673.
13. Manna M, Benocci C, Simons E. Large eddy simulation of turbulent flows via domain decomposition techniques. Part 1: Theory. *International Journal for Numerical Methods in Fluids* 2005; **48**:367–395.
14. Benocci C, Giammanco R, Manna M, Simons E. Large eddy simulation of turbulent flows via domain decomposition techniques. Part II: Applications. *International Journal for Numerical Methods in Fluids* 2005; **48**:397–422.
15. Tyagi M, Acharya S. Large eddy simulation of turbulent flows in complex and moving rigid geometries using the immersed boundary method. *International Journal for Numerical Methods in Fluids* 2005; **48**:691–722.
16. Kravchenko AG, Moin P, Moser R. Zonal embedded grids for numerical simulations of wall-bounded turbulent flows. *Journal of Computational Physics* 1996; **127**:412–423.
17. Namkoong K, Choi HG, Yoo JY. Computation of dynamic fluid–structure interaction in two dimensional laminar flows using combined formulation. *Journal of Fluids and Structures* 2005; **20**:51–69.
18. Sarrate J, Huerta A, Donea J. Arbitrary Lagrangian–Eulerian formulation for fluid–rigid body interaction. *Computer Methods in Applied Mechanics and Engineering* 2001; **190**:3171–3188.
19. Souli M, Ouahsine A, Lewin L. ALE formulation for fluid–structure interaction problems. *Computer Methods in Applied Mechanics and Engineering* 2000; **190**:659–675.
20. Weaver DS. Ziada S, Au-Yang MK, Chen SS, Paidoussis MP, Pettigrew MJ. Flow-induced vibration in power and process plants components—progress and prospects. *Journal of Pressure Vessel Technology* (ASME) 2000; **122**:339–348.
21. Blevins RD. *Flow Induced Vibrations* (2nd edn). van Nostrand Reinhold: New York, 1990.
22. Bathe KJ, Wilson EL. *Numerical Methods in Finite Element Analysis*. Prentice-Hall: Englewood Cliffs, NJ, 1976.
23. Piomelli U. *Large-eddy and Direct Simulation of Turbulent Flows*, *a CFD Odyssey*. Report of Department of Mechanical Engineering, University of Maryland, U.S.A., 2001.
24. Germano M, Piomelli U, Moin P, Cabot WH. A dynamic subgrid scale eddy viscosity model. *Physics of Fluids* 1991; **3**:1760–1765.
25. Patankar SV. *Numerical Heat Transfer and Fluid Flow*. McGraw-Hill: New York, 1980.
26. Zhang H *et al*. Recent development of fluid–structure interaction capabilities in the ADINA system. *Computers and Structures* 2003, **81**:1071–1085.
27. Zhang LX, Wang WQ, Guo YK. Study on intrinsic features of turbulent flow in strong 3D skew blade passage for a Francis turbine. *Journal of Hydrodynamics*, *Series B* 2006; **18**(6).
28. Qian WC. *Generalized Variational Principle* (in Chinese). Knowledge Press: Beijing, 1985.

DOI: 10.1002/fld